

Optimal Energy Management in Autonomous Power Systems with Probabilistic Security Constraints and Adaptive Frequency Control

Spyridon Chapaloglou, Erick Alves, *Senior Member, IEEE*, Vincenzo Trovato, *Member, IEEE*, and Elisabetta Tedeschi, *Senior Member, IEEE*

Abstract—The decarbonization of many heavy power-consuming industries is dependent on the integration of renewable energy sources and energy storage systems in isolated autonomous power systems. The optimal energy management in such schemes becomes harder due to the increased complexity and stability requirements, the rapidly varying operating conditions and uncertainty of renewable sources, the conflicting objectives across different timescales, the limited amount of reliable power sources and energy storage. The state of charge management when energy storage is used for multiple services, such as optimal scheduling and frequency support, is one of the most notorious problems in this context. To address this issue, an optimal energy management system is proposed in this paper. It co-optimizes the primary frequency control layer and the dispatch schedule of conventional generators and energy storage by taking advantage of an algorithm that provides adaptive active power demand uncertainty quantification, theoretical guarantees for frequency stability, and bounds for the reserves for frequency support assigned to the energy storage system. A pattern-based reformulation of the frequency stability constraints is derived enabling the efficient solution of the involved optimization problem, being a test case of an isolated offshore oil and gas platform presented for validation.

Index Terms—power generation dispatch, energy management, load forecasting, power system stability, adaptive control.

NOMENCLATURE

Sets

$t \in \mathbb{Z}_+$	time index (scheduling time scale).
$k \in \mathcal{K}$	prediction horizon (discrete time domain).
$g \in \mathcal{N}_g$	set of generators.
$b \in \mathcal{N}_b$	set of batteries.
$\delta \in \Delta$	set of net load samples.
$i \in N$	set of net load sample indices.
$j \in \mathcal{J}$	set of configurations.
$n \in \mathcal{T}$	set of trees in a random forest.

This research was funded by: 1) VISTA - a basic research program in collaboration between The Norwegian Academy of Science and Letters, and Equinor; 2) the Onassis Foundation - Scholarship ID: F ZP 056-1/2019-2020; 3) the Research Council of Norway under the program PETROMAKS2, grant number 281986, project “Innovative Hybrid Energy System for Stable Power and Heat Supply in Offshore Oil and Gas Installation (HES-OFF)”.

S. Chapaloglou, E. Alves, and E. Tedeschi are with the Department of Electric Power Engineering, Norwegian University of Science and Technology, 7034 Trondheim, Norway, e-mail: (see <https://www.ntnu.edu/employees/spyridon.chapaloglou>). V. Trovato is with the Department of Civil, Environmental and Mechanical Engineering at University of Trento, 38123 Trento, Italy and with the Department of Electrical and Electronic Engineering at Imperial College London, London SW7 2BX, United Kingdom. E. Tedeschi is also with the Department of Industrial Engineering, University of Trento, 38123 Trento, Italy.

\mathcal{D}_k^p	datasets.
Superscripts	
b	battery.
gt	gas turbine.
nl	net load.
ch	charging.
dis	discharging.
p	random variable indicator, $p = \ell$ for load, $p = w$ for wind power.
f	frequency bound.
e	energy bound.
Parameters	
T	scheduling (long-term) time step [min].
S_b	system base power [MW].
t_0	time at the beginning of the prediction interval [s].
t'_0	time at active power perturbation realization [s].
r_{ss}	steady state frequency deviation limit [pu].
r_{tr}	transient state frequency deviation limit [pu].
$\bar{\gamma}$	maximum rate of change of frequency [pu/s].
λ	energy deviation margin [%].
\bar{E}^b	battery energy capacity [MWh].
\bar{P}^b	battery power rating [MW].
\bar{x}^{SoC}	maximum state of charge.
\underline{x}^{SoC}	minimum state of charge.
\bar{P}^{gt}	gas turbine maximum power [MW].
\underline{P}^{gt}	gas turbine minimum power [MW].
Binary variables	
s	battery discharging indicator.
b	configuration indicator.
x^{gt}	gas turbine status (on/off).
Continuous variables	
t	time [s].
\mathcal{X}	system frequency (centre of inertia) [pu].
P	power [MW].
ΔP	power reserves [MW].
P_b	power perturbation [pu].
M	unit inertia [s].
\mathcal{M}	system inertia [s].
D	unit damping [pu].
\mathcal{D}	system damping [pu].
x^{SoC}	state of charge [-].
E	state of energy [MWh].
ΔE	energy variation [MWh].

\mathbf{x}	control system states.
\mathbf{z}	variables capturing economic costs of operation.
\mathbf{u}	control inputs (power and status commands).
\mathbf{v}	control inputs (droop and virtual inertia coefficients).
ξ	uncertain disturbance (net load).
$X_{d,k}^p$	input features.
$P_{d,k}^p$	k^{th} step ahead load/wind power (observations).
P_{t+k}^p	random variable (load/wind power).
$\hat{P}_{t+k}^p(x)$	estimated conditional expected value of random variable (load/wind power).
$\hat{F}_{t+k}^p(x)$	estimated conditional cumulative distribution function of random variable (load/wind power).
$Q_{\tau,k}^p(x)$	estimated conditional quantiles of random variable (load/wind power).
$\hat{F}_K^p(x)$	estimated conditional multi-variate cumulative distribution function of random variable (load/wind power).

ABBREVIATIONS

APD	active power disturbance.
APS	autonomous power system.
BPS	bulk power system.
CAPEX	capital expenditure.
CDF	cumulative distribution function.
COI	center of inertia.
ED	economic dispatch.
EMS	energy management system.
ESS	energy storage system.
GT	gas turbine.
MILP	mixed integer linear programming.
MPC	model predictive control.
O&G	oil and gas.
OPEX	operational expenditure.
PFC	primary frequency control.
RES	renewable energy source.
RF	random forest.
RoCoF	rate of change of frequency.
SoE	state of energy.
UC	unit commitment.

I. INTRODUCTION

TAKING optimal decisions to reduce *i)* fuel consumption, *ii)* greenhouse gases emissions, *iii)* equipment degradation and *iv)* system insecurity in power systems with a high share of **renewable energy sources (RESs)** is an intricate task. This endeavor requires the solution of problems such as the **unit commitment (UC)** [1], **economic dispatch (ED)** [2], and allocation of reserves for frequency control [3], resulting in complex non-convex optimization formulations. Those have typically conflicting objectives, continuous and binary decision variables, and high uncertainty from particular nodes, such as loads and **RESs**. Reliability can, for instance, be increased

where more dispatchable units, such as **gas turbines (GTs)**, are kept online for longer periods, as they respond well to fast variations of loads and **RESs**. This action may, however, increase fuel consumption, emissions, and equipment degradation, affecting negatively **operational expenditure (OPEX)**.

When compared to traditional **bulk power systems (BPSs)**, this type of optimization can have different characteristics in **autonomous power systems (APSs)**, such as isolated industrial plants, **oil and gas (O&G)** platforms, ships, islands, and community microgrids. Due to the size and complexity of the problem, several challenges exist in **BPSs** to implement real-time, advanced algorithms for optimal dispatch and real-time allocation of frequency reserves [4]. Such problems can however be addressed in many **APSs** due to the limited number of dispatchable power sources, which typically provide simultaneously several ancillary services. The methods for allocation of frequency reserves and tuning of the system damping may also differ considerably between **BPS** and **APS**. The system damping is, in the former, adapted using binary decision variables which switch on and off units having a fixed active power-frequency droop, as usually the individual contribution of each unit to the total damping is small. In the latter, the droop of individual units may represent a large portion of the system damping, being therefore necessary to readjust them in real-time using integer variables to obtain optimal results.

Optimization objectives and decisions in **APSs** may also be coupled and affected by constraints in different time scales, being **energy storage systems (ESSs)** remarkable examples of equipment that enhances such dependencies. **ESSs** can, for instance, provide increased flexibility towards the optimal scheduling of fossil-based energy sources and avoid prolonged operation in partial loads, where emissions are much higher. They can also be assigned as spinning reserves for frequency control, which would require less **GTs** on for the same system security requirements and increase environmental gains even further. Where these two grid services are provided simultaneously, the scheduled trajectory of the **ESS' state of energy (SoE)** may be disturbed, affecting the optimality or even the feasibility of the original schedule. To decide in **BPSs** the effect that the provision of frequency reserves has on the **ESS' optimal schedule**, scenarios such as the worst-case **active power disturbance (APD)** or the N-1 criterion are many times used [3], [5]. These criteria can however be over-conservative in **APSs** [6] and the **capital expenditure (CAPEX)** necessary for a fully-fledged **ESS** may not justify its benefits, being some probability of load shedding and generation curtailment acceptable many times [7]. When it comes to energy management in **APSs** with high penetration of **RES**, there is therefore a need and potential for better assessment of frequency stability requirements as well as coordination and scheduling of reserves.

A. Literature review

The integration of frequency stability constraints in the scheduling phase of **BPSs** with high penetration of **RES** has been an active area of research in recent years and is well

described in the literature [8]. The use of linear constraints had been a typical approach to increase the fidelity of the frequency response in the UC and ED problems, which are obtained by linearizations and/or analytical solutions of the swing equation model [9]–[16]. These procedures provide good approximations in BPSs, where the largest APD is a small fraction of the installed capacity and transient and steady-state frequency deviations are usually required to be below 2% of its rated value [5]. Frequency deviations may, on the other hand, be much higher in APS due to low inertia and limited amount of frequency reserves when compared to the worst-case APDs, causing the effects of non-linear dynamics to be sizeable during large disturbances [17]. Where these non-linear effects are considered, bilinear terms are introduced in the frequency stability constraints, those requiring specialized reformulation-linearization techniques [18]–[20]. This increase of the optimization model complexity can play an important role in APS, while it may bring only negligible frequency stability improvements in BPS.

The challenge of leveraging optimal system operation and security in APSs was also addressed recently, being alternatives presented to the deterministic evaluation of the worst-case APD or the N-1 criterion. References [13], [21]–[24], for instance, considered the effect of anticipated net load variations and applied dynamic constraints for sizing frequency containment reserves and required inertia. These works did not evaluate however the impact that re-adjusting the droop of online units, instead of switching on and off units with fixed droops, would have on frequency stability and OPEX. References [9], [15], [20], [25] tried moreover to tackle the problem by applying simplified and static uncertainty models, such as non adaptive and arbitrary uncertainty intervals, distributions, and scenario selection, which have the limitation of not providing probabilistic guarantees.

B. Paper contributions

The main contribution of this paper is an algorithm for the energy management system (EMS) of a generalized APS equipped with an ESS that is capable of simultaneously achieving optimal scheduling and securing system operation under dynamic uncertainty considerations and bounded impact on its optimal scheduling. The proposed algorithm introduces a particular set of frequency constraints with general applicability, those not being limited to small-scale power variations. Compared to the formulation based on the linearized swing equation traditionally adopted in frequency-constrained UC (e.g., [10], [18]), our formulation is robust to large frequency deviations around the system equilibrium point. This is an important feature for APSs, which are often subject to larger frequency deviations than BPSs. Likewise, this feature might be key in future BPSs dominated by power electronic converters. Such constraints are combined with a probabilistic security framework based on a novel adaptive APD uncertainty quantification scheme. Additional novel energy constraints to frequency reserves (inertial and primary) provided by an ESS are derived, bounding the impact of the uncertain grid service provision on the optimal schedule. This new method allows

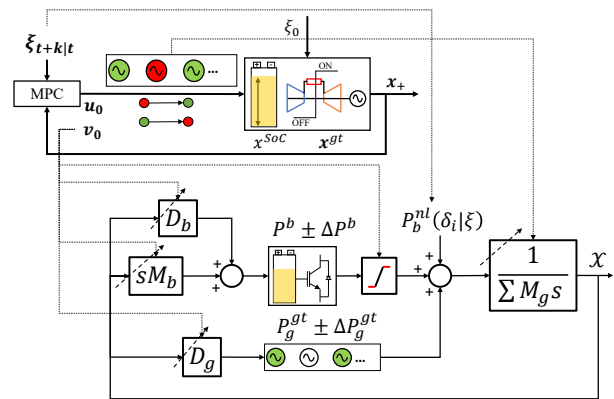


Fig. 1. Hierarchical control system schematic where the upper layer optimal discrete time control is integrated with the lower time scale continuous adaptive primary frequency control.

an EMS to allocate time-varying optimal frequency control reserves with bounded divergence from its optimal SoE. A simple strong mixed integer linear programming (MILP) reformulation is derived to efficiently implement the proposed algorithm, whose effectiveness is verified by simulations using the case study of a wind-powered offshore O&G platform.

In summary, we propose an EMS for APSs with the following novel features:

- adaptive APD uncertainty quantification with probabilistic guarantees for frequency-constrained energy management
- integration of frequency stability constraints into the optimal scheduling that consider non-linear frequency dynamics and are valid for large frequency deviations
- energy constraints bounding the impact of uncertain frequency support provision (inertial and primary) by an ESS, on its optimal SoE schedule

The rest of the paper is organized as follows. The proposed EMS algorithm and its numerical implementation are presented in Section II, while simulations in Matlab/Simulink are used to validate and discuss the various features of the proposed algorithm using the case study of a wind-powered offshore O&G platform in Section III. The main conclusions are finally presented in Section IV.

II. METHOD

The concept and the methodology proposed in this paper is presented in detail in this section. It assumes the existence of a centralized EMS in an APS that is capable not only to dispatch a set of g generators and a single ESS b , but also to decide, for the primary frequency controllers, the proportional gain (droop) D_g of each generator, the proportional gain (droop) D_b and derivative gain (virtual inertia) M_b of the ESS. Fig. 1 shows a conceptual illustration of the proposed scheme for the hierarchical EMS. The set v_0 represents the control inputs to the low-level primary frequency controllers, which include droop and virtual inertia coefficients, and is embedded into the set of commands u_0 from the EMS. The latter also includes the decisions to startup (green circles) or to shutdown (red circles) the GTs. The techno-economic optimal schedule included in

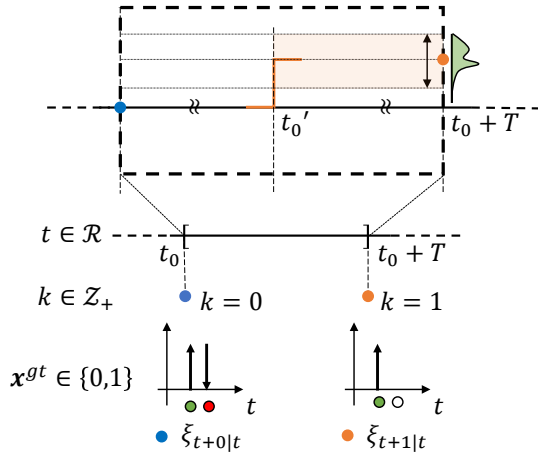


Fig. 2. Visualization of the proposed adaptive and probabilistic step-like net active power disturbance quantification at a time instant in the continuous range between the discrete points in time where decisions are taken.

u_0 not only shall be feasible for the actual net load disturbance ξ_0 at $t = t_0$, but also will define the inertial support $\sum_g M_g$ of conventional generators during $[t_0, t_0 + T]$, where T is the time step of the scheduling, further complicating the frequency control problem.

Note that the commands u_0 are given for discrete points of the time interval (i.e., $k = 0 \Rightarrow t = t_0$ and $k = 1 \Rightarrow t = t_0 + T$) based on the discrete net load forecasts ($\xi_{t+0|t}$, $\xi_{t+1|t}$). The transition from $\xi_{t+0|t}$ to $\xi_{t+1|t}$, however, can happen at any time in the continuous time interval $[t_0, t_0 + T]$. In the proposed EMS algorithm, the power reserves ΔP_g^{gt} and ΔP_b are decided in an adaptive way respecting the ESS SoE bounds. The forecast net load values $\xi_{t+k|t}$ at time t , along with their corresponding uncertainties, are used to characterize the potential APDs $P_b^{nl}(\delta_i | \xi)$ that can occur in the interval $[t_0, t_0 + T]$. This is illustrated in Fig. 2, where the APD came off at a time $t_0 \leq t'_0 \leq t_0 + T$. As the forecasts are uncertain, the APD amplitude belongs to a value range (orange region), being therefore a function of the underlying probability density (green area) at the next scheduling instance $k = 1 \Rightarrow t = t_0 + T$. Where this probabilistic quantification algorithm is applied, the frequency control parameters D_g , D_b , M_b to be implemented in the current time instance $t = t_0$ through the command v_0 are decided in an adaptive way. This algorithm is further detailed in Sections II-C and II-D.

A. Frequency Control and Reserves Allocation

The non-linear dynamics of the frequency deviation for the center of inertia (COI) in an ac power system are given in Eq. (1), where $\mathcal{X} = \frac{\omega}{\omega_s}$, and ω, ω_s are the COI frequency and its rated value respectively.

$$\dot{\mathcal{X}} = \frac{\mathcal{D}}{\mathcal{M}} (\mathcal{X} - 1) + \frac{P_b^{nl}}{\mathcal{X}\mathcal{M}} \quad (1)$$

$$\mathcal{D} \geq \frac{P_b^{nl}}{r_{ss}(1 - r_{tr})} \quad (2)$$

$$\mathcal{M} \geq \frac{P_b^{nl}}{\bar{\gamma}} \quad (3)$$

It is shown in [17] that if the total system damping \mathcal{D} is selected as in Eq. (2), then \mathcal{X} will be bounded post-disturbance by r_{ss} for an instantaneous net active power imbalance P_b^{nl} , where r_{tr} is a pre-defined constant bound for the nadir/zenith of \mathcal{X} during the transient period. Note that the step-response of frequency for active power disturbances is, in most ac power systems, underdamped due to delays of actuators and their non-linearities [26]. Those effects are not modelled in Eq. (1) because they influence only the frequency nadir or zenith after the disturbance P_b^{nl} occurs, being the post-disturbance steady-state value of \mathcal{X} unaffected [17]. The variables r_{ss} and r_{tr} in Eq. (2) represent, in other words, the allowed steady-state and transient frequency deviations in per unit of \mathcal{X} , being usually defined in grid codes or by the system operator.

It is typical to assume $r_{tr} > r_{ss}$ to provide a safety margin which avoids triggering protection schemes such as under frequency load shedding or over frequency generation curtailment during large disturbances. When $r_{ss} = r_{tr}$, there exists no safety margin between steady-state and transient values. It shall also be noted that Eq. (2) is valid for any value of \mathcal{X} , and not only for small deviations around the operating point.

The minimum required inertia \mathcal{M} is retrieved from Eq. (1), assuming that a) the disturbance P_b^{nl} occurs at $t = t'_0$, b) the system was previously in balance ($\mathcal{X}|_{t=t'_0} = 1$), and c) the maximum rate of change of frequency (RoCoF) is $\dot{\mathcal{X}}|_{t=t'_0} = \bar{\gamma}$, which results in Eq. (3).

Ensuring that enough power reserves are available in an APS is a necessary condition to satisfy the constraints for frequency control imposed by Eqs. (2) and (3). The values of \mathcal{D} and \mathcal{M} depend on the number of online units and their individual parameters, being expressed by Eqs. (4) and (5), where D_g and M_g denote the droop setting and the inertia of each online generator, and D_b and M_b are the virtual damping and inertia emulated by the ESS, respectively. The EMS must guarantee that each individual equipment has enough available power capacity to provide the frequency reserves assigned to it, what leads to the constraints in Eqs. (6) and (7).

$$\mathcal{D} = \sum_g^{N_g} x_g^{gt} D_g + D_b \quad (4)$$

$$\mathcal{M} = \sum_g^{N_g} x_g^{gt} M_g + M_b \quad (5)$$

$$|\Delta P_b(t)| \leq M_b \bar{\gamma} + D_b r_{tr} \quad (6)$$

$$|\Delta P_g(t)| \leq x_g^{gt} D_g r_{tr}, \quad \forall g \in \mathcal{N}_g \quad (7)$$

B. Optimal and Bounded Energy Management under Uncertainty

1) *Allocation of frequency reserves with bounded energy storage:* The EMS must also ensure that enough energy capacity is available in the ESS. This is required not to violate the storage limits when providing frequency control in the current scheduling step t_0 while charge or discharge events had already been scheduled for the next step $t_0 + T$, where T is the time step of the EMS. To deal with this situation, the

constraint in Eq. (8) is proposed, where $\Delta E^b(t)$ is a deviation around the optimal scheduled SoE $E^b(t)$, and λ is a user-defined (absolute) percentage value that enables the system operator to define the tolerable departure from the optimal reference SoE schedule. The proposed constraint allows, in other words, an allocation of frequency reserves to the ESS that is proportional to its current energy level.

$$\Delta E^b(t) \leq \overline{\Delta E^b}(t) = \lambda E^b(t) \quad (8)$$

For energy calculations of frequency containment reserves in EMS algorithms, one can assume that $\mathcal{X} \leq r_{ss}$, $\forall t \in [t_0, t_0 + T]$ when the system is frequency stable [17], this simplification resulting in Eq. (9). Remark that, on one hand, $r_{ss} \leq \mathcal{X} \leq r_{tr}$ during the arrest and rebound periods of frequency containment. On the other hand, those periods combined last only a couple of seconds, while T may vary from 5 minutes to 15 minutes in typical EMSs. The integration error would therefore be minimal when adopting this simplification. The latter however allows $\overline{\Delta E^b} \leq \Delta E^b(t)$ to be enforced in the optimization problem, as described later in Section II-C, and to satisfy Eq. (8), which avoids excessive deviations of the SoE from its optimal dispatch.

$$\begin{aligned} \Delta E^b(t) = \Delta E^b(\mathcal{X}) &= \int_{t_0}^{t_0+T} (M_b \dot{\mathcal{X}} + D_b \mathcal{X}) dt = \\ M_b \mathcal{X} \Big|_{t_0}^{t_0+T} + D_b \int_{t_0}^{t_0+T} \mathcal{X} dt &\leq M_b r_{tr} + D_b r_{ss} T = \overline{\Delta E^b} \end{aligned} \quad (9)$$

2) *Adaptive Uncertainty Quantification:* Load uncertainty is, in the proposed method, evaluated not only in rapidly varying loads but also in the intermittency of non-dispatchable power sources, being the net load variation defined as the combination of two random variables P^p , where $p = \{\ell, w\}$ corresponds to load and non-dispatchable sources respectively. To achieve adaptive quantification of the uncertainty for a given prediction horizon \mathcal{K} , it is sufficient to estimate a time-dependent (conditional) multivariate cumulative distribution function (CDF) $\hat{F}_{\mathcal{K}|t}^p$ [27]. Ensembles of random forest (RF) models [28] can, therefore, be assembled together to perform multi-step ahead predictions given available datasets $\mathcal{D}_k^p = \{X_{d,k}^p, P_{d,k}^p\}_{d=1:N_D}, \forall k \in \mathcal{K}$, where $X_{d,k}^p$ are the input features and $P_{d,k}^p$ the available observations for regression representing realizations of each random variable P^p at the k^{th} step ahead. For that, individual RF models are trained for each variable P^p and lead time $k \in \mathcal{K}$. Each RF is composed of $|\mathcal{T}|$ auto-regressive trees $f_{n,k}^p(\cdot)$, $n \in \mathcal{T}$. The inputs to the trees (regressors) $\mathbf{x}_r(t)$ are composed only by the current ($k=0$) and L lagged values of the corresponding variable, that is $\mathbf{x}_r(t) = [P_t^p, P_{t-1}^p, \dots, P_{t-L}^p]^T \forall p = \{\ell, w\}$. Following the procedure described in [27], a point forecast can be calculated for the corresponding prediction horizon \mathcal{K} using Eq. (10), where $\mathbb{1}\{\cdot\}$ is the indicator function operator, N_D the number of observations $P_{d,k}^p$ in the corresponding training datasets, and $\mathcal{S}_{n,k}(\mathbf{x}_r)$ is the leaf node of the corresponding tree n and RF model k in which the new input $\mathbf{x}_r(t)$ falls in.

$$\begin{aligned} \hat{P}_{t+k}^p(\mathbf{x}_r(t)) &= \frac{1}{|\mathcal{T}|} \sum_{n \in \mathcal{T}} f_{n,k}^p(\mathbf{x}_r(t)) \quad \forall k \in \mathcal{K}, p = \{\ell, w\} \\ f_{n,k}^p(\mathbf{x}_r(t)) &= \sum_{d=1}^{N_D} \frac{\mathbb{1}\{X_{d,k}^p \in \mathcal{S}_{n,k}(\mathbf{x}_r(t))\}}{N_D} P_{d,k}^p \Rightarrow \\ f_n^p(\mathbf{x}_r(t)) &= \sum_{d=1}^{N_D} \tau_{d,k}(\mathbf{x}_r(t)) P_{d,k}^p \quad \forall k \in \mathcal{K}, p = \{\ell, w\} \end{aligned} \quad (10)$$

From Eq. (10), the conditional expected value $\hat{\mathbb{E}}[P_{t+k}^p | \mathbf{x}_r(t)]$ of each random variable and lead time can be expressed by the corresponding estimates \hat{P}_{t+k}^p as a function of time [29]. Time-varying CDFs $\hat{F}_{t+k|t}^p$ can also be inferred [29] for each random variable and lead time as in Eq. (11), besides the time-varying estimates of the expectations which can be considered a ‘‘mean’’ multi-step ahead prediction. It is shown in [27] that, using Eq. (11), the multi-variate $\hat{F}_{\mathcal{K}|t}^p$ can be approximated by sampling of the marginals $\hat{F}_{t+k|t}^p$. By combining the random variables P_{t+k}^p for $p = \{\ell, w\}$, the net load can be also represented as a time-dependent random variable as $\xi_{t+k}(t) = P_{t+k}^\ell(t) - P_{t+k}^w(t)$ which encapsulates the system disturbance uncertainty for the EMS.

$$\begin{aligned} \hat{F}_{t+k|t}^p &= \frac{1}{|\mathcal{T}|} \sum_{n \in \mathcal{T}} \sum_{d=1}^{N_D} \tau_{d,k}(\mathbf{x}_r(t)) \mathbb{1}\{P_{d,k}^p \leq P_{t+k}^p\} \Rightarrow \\ P_{t+k}^p &\sim \hat{F}_{t+k|t}^p(P_{t+k}^p | \mathbf{x}_r(t)), \quad \forall k \in \mathcal{K}, p = \{\ell, w\} \end{aligned} \quad (11)$$

Any decision taken by a predictive EMS algorithm relying on that forecast will however be sub-optimal, as the net load ξ_0 that actually hits the system at $t = t_0$ (see Fig. 2) is a realization of the random $\xi_{t+k}(t)$. The latter is, in principle, different from the forecasted value due to inevitable forecasting errors, a fact that not only degrades the optimality of the decision in terms of economic value but most importantly is critical to evaluate the APDs which may threaten the system’s frequency stability due to insufficient inertia or damping. It is therefore important to quantify the uncertainty of the random net load $\xi(t)$ and subsequently of the APD that can occur in the interval $[t_0, t_0 + T]$. For the sake of brevity, this paper will not detail further the uncertainty quantification method, its validation, and how net load scenarios can be generated. The interested reader can however refer to [27] for a full description. Where the procedure described in [27] is applied, the uncertainty of the net load affecting an isolated APS can be quantified through the adaptive probabilistic forecasting framework described in this section. This procedure will be exploited in the construction of the security constrained energy management algorithm described in Section II-C.

C. Probabilistically Constrained EMS

This section presents how the proposed EMS algorithm integrates into a single optimization problem including the

various objectives and multiple time-scale requirements described in Sections II-A and II-B. The system dynamics are first expressed in a hybrid state space system to achieve this integration as shown in Eq. (12), where \mathbf{x}_+ is the state at the next discrete time, \mathbf{u} the corresponding control inputs and \mathbf{A}, \mathbf{B} the corresponding system matrices. Note that $x^{SoC} = \bar{E}^b / \bar{E}^b \in [\underline{x}^{SoC}, \bar{x}^{SoC}]$ and $\mathbf{x}_{1:N_g}^{gt} = \{x_g^{gt}\}_{1:N_g} \in \{0, 1\}$.

$$\mathbf{x}_+ = \mathbf{A}\mathbf{x} + \mathbf{B}\mathbf{u} \quad (12)$$

The optimization problem presented in Eq. (13) is then formulated and solved in each discrete time step t , where $\delta = \{\delta_k^i\}_{1:K}$ is a random multi-sample, $\xi = \{\xi_k\}_{0:K-1}$ is the deterministic mean net load forecast including the measured value ξ_0 at $t = t_0$, and $\mathbf{P}_b^{nl} = \{P_b^{nl}(\delta_{k+1}|\xi_k)\}_{0:K-1}$ is the net load perturbation for the whole prediction horizon \mathcal{K} as a function of the sample and the mean forecast. The control horizon was set to be equal to the prediction horizon \mathcal{K} , which is a common practice in model predictive control (MPC) schemes [30]. $|\mathcal{K}| = 6$ is used by the adaptive uncertainty quantification module explained in Section II-B2, being this value long enough to provide reliable forecasts to some quarters ahead but short enough to limit the additional computational burden and processing time for the EMS.

$$\mathcal{P} : \min_{\mathbf{u}, \mathbf{v}, \mathbf{z}} \{\mathcal{F}(\mathbf{x}_+, \mathbf{z}, \mathbf{u}, \mathbf{v}; \xi)\}$$

$$\text{where, } \mathcal{F} := \underbrace{\mathcal{J}(\mathbf{x}_+)}_{\text{states cost}} + \underbrace{\mathcal{J}(\mathbf{z})}_{\text{operation cost}} + \underbrace{\mathcal{J}(\mathbf{u})}_{\text{control cost}} + \underbrace{\mathbf{w}^T \mathbf{v}}_{\text{reserves cost}}$$

$$\text{s.t. } \mathcal{C}(\mathbf{x}_+, \mathbf{z}, \mathbf{u}, \mathbf{v}, \xi) \leq 0,$$

$$\begin{aligned} \mathbb{P}(\delta \in \Delta \mid |\xi - \delta| = \mathbf{P}_b^{nl} \leq \\ \min\{\mathcal{D}r_{ss}(1 - r_{tr}), \mathcal{M}\bar{\gamma}\}\mathbb{1}_{\{1:K\}}) \geq 1 - \epsilon. \end{aligned} \quad (13)$$

In the cost function \mathcal{F} , $\mathcal{J}(\mathbf{x}_+)$ represents the cost of having generators online, $\mathcal{J}(\mathbf{z})$ penalizes the deviation from optimal operating conditions of online generators and the ESS, $\mathcal{J}(\mathbf{u})$ captures the start up cost of generators, and finally $\mathbf{w}^T \mathbf{v}$ accounts for costs of activating reserves for frequency control. The decision variables $\mathbf{v} = [D_g, D_b, M_b]^T$ used for frequency reserves are weighted by \mathbf{w} so that different contributions can be assigned to online generators and the ESS to ensure the system frequency stability. In that aspect, the higher the numerical value of the corresponding \mathbf{w} element, the closer a generator will remain to its optimal operating point, as its contribution to frequency control is penalized. Each term of \mathcal{F} is described in detail in [27] and expresses the corresponding economical cost defined by coefficients such as GT startup cost, fuel consumption, battery cycling, and so on.

The term $\mathcal{C}(\cdot)$ encapsulates all the constraints related to the operation of the energy system, as described in [27]. The last expression in Eq. (13) is a chance constraint that, given the estimated distributions from Eq. (11), relates potential instantaneous perturbations for a net load value ξ_k and the next step sampled net load δ_{k+1}^i . Equations (2) and (3) are, in other words, risk-constrained by ϵ , which act as a mechanism to leverage cases with rather pessimistic prediction intervals resulting from poor uncertainty range estimation.

The chance constraint complicates, however, the optimization problem. Note that \mathcal{P} is a stochastic mixed integer nonlinear problem and therefore non-convex, so a standard *scenario approach* cannot be applied. Following [31], [32], a probabilistic set composed of a finite number of samples $\delta^i \in \Delta^N$ is computed as in Eq. (14), being β and e user defined parameters that tighten the non-violation of the original chance constraint. Note that the number of random variables is $2|\mathcal{K}|$ because two sources of uncertainty exist (load and renewable power injection) for the whole prediction horizon. The chance constraint can however be replaced by the deterministic set of linear inequalities presented in Eq. (15), which transforms the stochastic problem \mathcal{P} into a robust one, where the set Δ^N encapsulates the same risk-volume ϵ as the original chance constraint. When solving the corresponding robust program, solutions are not only feasible for the initial \mathcal{P} but also satisfy the same probabilistic guarantees [33].

$$N \geq \frac{1}{\epsilon} \frac{e}{e-1} \left(\ln \frac{1}{\beta} + 4|\mathcal{K}| - 1 \right) \quad (14)$$

$$|\xi - \delta^i| = \mathbf{P}_b^{nl} \leq \min\{\mathcal{D}r_{ss}(1 - r_{tr}), \mathcal{M}\bar{\gamma}\}\mathbb{1}_{\{1:K\}} \quad (15) \\ \forall \delta^i \in \Delta^N$$

D. MILP reformulation of frequency stability and bounded energy storage constraints

It is not feasible, on one hand, to implement the constraints expressed in Eqs. (2), (4) and (7) directly into a MILP formulation because of the bi-linear terms $x_g^{gt} D_g$. It is possible, on the other hand, to take advantage of the following observation: with N_g generators, there are exactly 2^{N_g} different possible system configurations depending on the values of $\mathbf{x}_{1:N_g}^{gt} \in \{0, 1\}$. The status variable $x_{g,t}^{gt}$ takes a particular value (0 or 1) for each generator and configuration, being therefore feasible to represent it by binary strings of length N_g . The feasible system configurations are then enumerated by taking all the possible permutations, which can be gathered in a data table $\mathbf{A}_{cf} [2^{N_g} \times N_g]$. The variables $x_{g,k}^{gt}, \forall k \in \mathcal{K}$ can, in this way, be treated as constants given a selected system configuration, being indicator variables b_j introduced to identify the configuration selected and associate it with the status of the generators by the set of constraints in Eqs. (16) and (17). Equation (4) can, as consequence, be linearized using \mathbf{A}_{cf} as in Eq. (18).

$$x_{g,k}^{gt} \geq b_j, \{(j, g) \in \mathcal{J} \times \mathcal{N}_g \mid [A_{cf}]_{j,g} = 1\} \quad (16)$$

$$x_{g,k}^{gt} \leq 1 - b_j, \{(j, g) \in \mathcal{J} \times \mathcal{N}_g \mid [A_{cf}]_{j,g} = 0\} \quad (17)$$

$$\mathcal{D} = \mathbf{A}_{cf} \mathbf{D}_g + D_b \mathbb{1}_{\{1:J\}} \quad (18)$$

With Equations (16) to (18) the initial *non-linear* formulation in Equations (1) to (7), which includes *bi-linear* terms, is translated into a set of equations appropriate for a MILP framework, and more precisely, one that has a good linear programming relaxation (strong formulation). Equations (2) and (3) can also be reformulated using the sampled net APD terms from Eq. (15). This is presented in Eq. (19), where M_B is a big-M value, $\mathbf{b}_k, \mathcal{D}_k$ correspond to each lead time of the

prediction horizon ($k \in \mathcal{K}$) assuming that M_g are constant values. The different possible configurations are restricted by a type 1 special ordered set constraint as in Eq. (20).

$$\mathbf{P}_b^{nl}(\delta_{k+1}^i | \xi_k) + M_B \mathbf{b}_k \preceq \mathcal{D}_k r_{ss} (1 - r_{tr}) + M_B \mathbb{1}_{\{1:J\}} \\ \frac{1}{\bar{\gamma}} \mathbf{P}_b^{nl}(\delta_{k+1}^i | \xi_k) \leq M_g \mathbb{1}_{\{1:N_g\}}^T \mathbf{x}_k^{gt} + M_{b,k} \quad (19)$$

$$\forall \delta_k^i \in \Delta^N, \forall k \in \mathcal{K} \\ \mathbb{1}_{\{1:J\}}^T \cdot \mathbf{b}_k = 1, \forall k \in \mathcal{K} \quad (20)$$

Equation (7) is similarly linearized using \mathbf{A}_{cf} and M_B as in Eqs. (21) and (22) where S_b is the system's base power.

$$\mathbf{P}_k^{gt} + M_B \mathbf{b}_k \preceq (\bar{P}^{gt} - D_{g,k} \cdot r_{tr} \cdot S_b) + M_B \mathbb{1}_{\{1:J\}}, \\ (\underline{P}^{gt} + D_{g,k} \cdot r_{tr} \cdot S_b) + M_B \mathbf{b}_k \preceq \mathbf{P}_k^{gt} + M_B \mathbb{1}_{\{1:J\}} \quad (21) \\ \forall k \in \mathcal{K}, \{(j, g) \in \mathcal{J} \times N_g \mid [A_{cf}]_{j,g} = 1\}$$

$$\mathbf{P}_k^{gt} + M_B \mathbf{b}_k \preceq M_B \mathbb{1}_{\{1:J\}}, \\ M_B \mathbf{b}_k \preceq \mathbf{P}_k^{gt} + M_B \mathbb{1}_{\{1:J\}}, \quad (22) \\ \forall k \in \mathcal{K}, \{(j, g) \in \mathcal{J} \times N_g \mid [A_{cf}]_{j,g} = 0\}$$

The **ESS** reserves from Eq. (6) are reformulated in terms of discharging and charging power as in Eq. (23), where s_k is the discharging binary indicator variable.

$$P_k^{dis} \leq s_k \bar{P}^b, \\ P_k^{dis} \leq \bar{P}^b - (D_{b,k} \cdot r_{tr} + M_{b,k} \cdot \bar{\gamma}) \cdot S_b, \quad (23) \\ P_k^{ch} \leq (1 - s_k) \bar{P}^b, \\ P_k^{ch} \leq \bar{P}^b - (D_{b,k} \cdot r_{tr} + M_{b,k} \cdot \bar{\gamma}) \cdot S_b, \forall k \in \mathcal{K}$$

The bound derived in Eq. (9) can be easily integrated to \mathcal{P} through the linear constraints in Eq. (24), where $\nu = \frac{r_{ss} S_b}{3600 \bar{E}^b}$.

$$\nu (M_{b,k} + D_{b,k} T) \leq \\ \min\{\bar{x}^{SoC} - x_{k-1}^{SoC}, x_{k-1}^{SoC} - \underline{x}^{SoC}, \lambda x_k^{SoC}\}, \quad \forall k \in \mathcal{K} \quad (24)$$

Equation (13) may therefore be expressed as a deterministic MILP robust program and solved efficiently by the **EMS** at each time iteration, as $\mathcal{F}(\cdot)$ and $\mathcal{C}(\cdot)$ can be expressed as linear combinations of the optimization variables when including the reformulations proposed in Eqs. (15) to (24).

III. SIMULATIONS

The various components of the proposed methodology are demonstrated in this section, namely the adaptive uncertainty quantification and the integration of frequency stability constraints with bounded use of the **ESS** stored energy in the optimal scheduling. To achieve this goal, the case study of a wind-powered offshore **O&G** platform is presented, where a reference operation time period is considered (8 hours) involving both regions of smooth, low magnitude and sudden, large net load variations. The reference isolated **APS** is composed of 4 identical **GTs** ($N_g = 4$) with $\bar{P}^{gt} = 1.09 \cdot 20.2$ MW, $\underline{P}^{gt} = 0.2 \cdot 20.2$ MW and a single battery **ESS** ($N_b = 1$) with $\bar{E}^b = 20$ MW h, $\bar{P}^b = 10$ MW, $\bar{x}^{SoC} = 0.8$, $\underline{x}^{SoC} = 0.2$.

Reference [27] presents the remaining parameter values and model details of this benchmark system. The effectiveness of the proposed methodology is demonstrated using time domain simulations of a 8 h period, corresponding to the complete scheduling time scale, and a simulation step of $T = 15$ min. The optimization problem is solved with *Gurobi 9.1.0* in a 28 physical core multi-node cluster with Intel(R) Xeon(R) CPU E5-2690 v4 @ 2.60 Hz and 25 GB RAM. The solution time of Eq. (13) using the proposed formulation is well below 15 minutes, which is assumed here as the minimum threshold for real-time power system scheduling.

A. Capabilities of adaptive uncertainty quantification

A representative example of how the adaptive uncertainty quantification framework works is illustrated in Fig. 3, where a case of a sudden **APD** was selected since these are the most interesting from a power imbalance perspective. The actual load values p^ℓ are presented with the solid black line and the blue cross ($p_{t|t}^\ell$) indicates the time instant at which a probabilistic forecast is issued. As described in Section II-B2, the probabilistic forecasts are composed of the expected values $\hat{E}[P_{t+k}^\ell | \mathbf{x}_r(t)]$ of the random variable P^ℓ , plotted with solid red line, and the prediction intervals $\hat{\alpha}(x)$ plotted around them in different shades of green, depending the quantile level $\tau = \{20\%, 40\%, 60\%, 80\%, 90\%\}$, for the whole prediction horizon ($k \in \mathcal{K}$). Two extreme quantile values $Q_\tau^\ell(\mathbf{x}_r(t))$ (for $\tau = \{5\%, 95\%\}$) are plotted with solid green lines, to illustrate that, as expected, most of the randomly generated sample values of load δ^i fall inside those. The random load samples δ^i are plotted in pink dots and represent one out of two components used for the net load scenarios. These scenarios are fed into the optimization problem \mathcal{P} through Eq. (15), being only 100 of them plotted in Figs. 3a to 3g for the sake of visualization clarity).

The proposed adaptive uncertainty quantification algorithm generates samples that better describe the size of an **APD** as a function of time. Observe that the prediction intervals $\hat{\alpha}$ and quantiles Q_τ^ℓ adapt to capture the irregular event of the sudden load increase as the blue cross moves forward in time (i.e., time t is updated from $t_0 - 3$ towards $t_0 + 3$), and a new forecast is issued from $p_{t|t}^\ell$ for the prediction horizon $t + k | t$. Note also that, at the initial time $t = t_0 - 3$ (Fig. 3a), the prediction intervals are narrow and all the sampled values δ^i (pink dots) fall close and around the actual load values. For the following intervals (i.e., $t = t_0 - 2, \dots, t_0 + 3$, Figs. 3b to 3g), however, the uncertainty increases and the prediction intervals $\hat{\alpha}$ and quantiles Q_τ^ℓ expand to capture the possibility of an irregular sudden load increase. Observe that, at the intervals prior to the **APD**, random load samples δ^i (pink dots) were generated at higher load values in the prediction horizon and close to the actual step (solid black line). The deterministic forecast (solid red line) which expresses the expected predictions ($\hat{E}[P_{t+k}^\ell | \mathbf{x}_r]$), in contrast, fails to capture the variation adequately, because it is dominated by the inertia of past values (lagged load values in $\mathbf{x}_r(t)$), a common drawback of auto-regressive models.

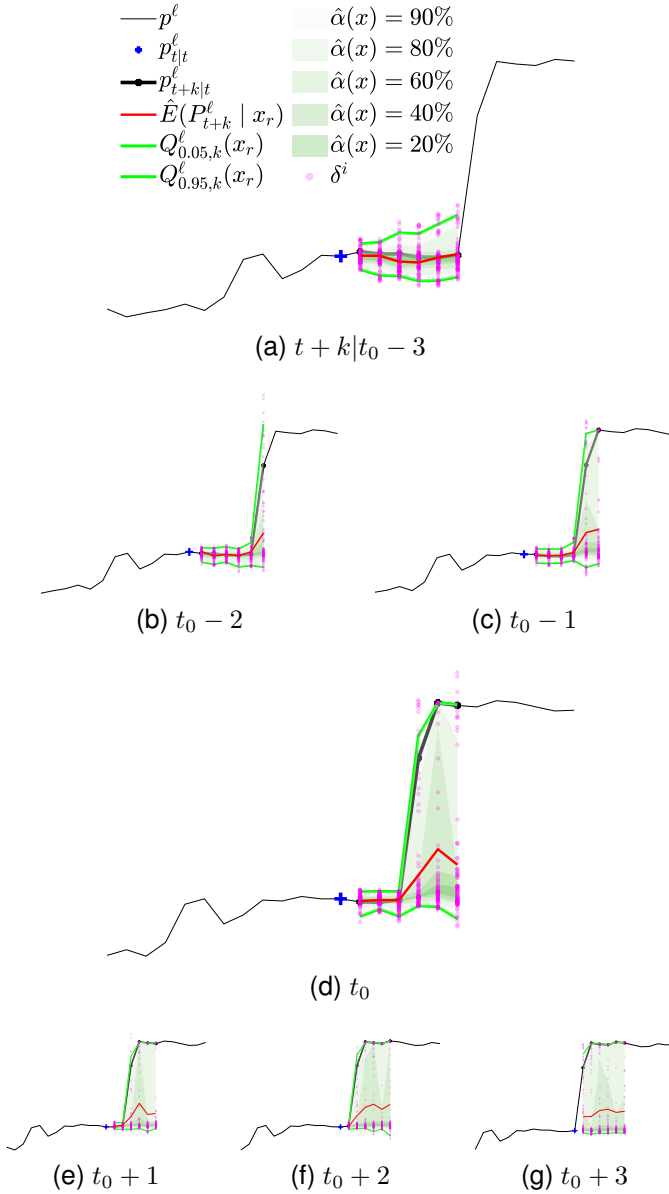


Fig. 3. Demonstration of adaptive uncertainty quantification by using autoregressive probabilistic forecasting for the load time-series. A case for a sudden step-like variation is presented for consecutive lead times (Figs. 3a to 3g). By updating the estimated prediction intervals it is possible to capture the sudden load variation and draw samples (purple dots) that span an appropriate range of values.

B. Effect of optimal and bounded frequency support from ESS

To demonstrate the effect of optimally controlling the ESS to provide frequency support for an isolated APS, a step APD is considered at time $t'_0 = 2s$ representing a 0.4 pu load increase from a sudden motor startup, where a single GT is on in the platform of the case study. Simulations were run in Matlab/Simulink 2022a using the model given in Eq. (1), which do not include delay of actuators. This simplification facilitates the interpretation of results, not implying however any loss of generality.

Results are illustrated in Fig. 4, where the frequency deviation (solid lines) and the RoCoF (dashed lines) for two cases are represented. In the first case (grey lines), the single

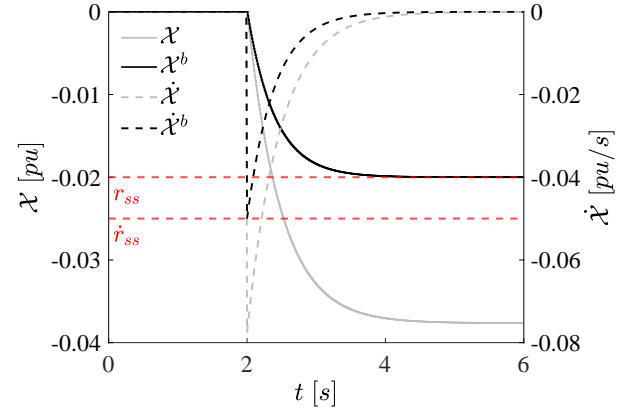
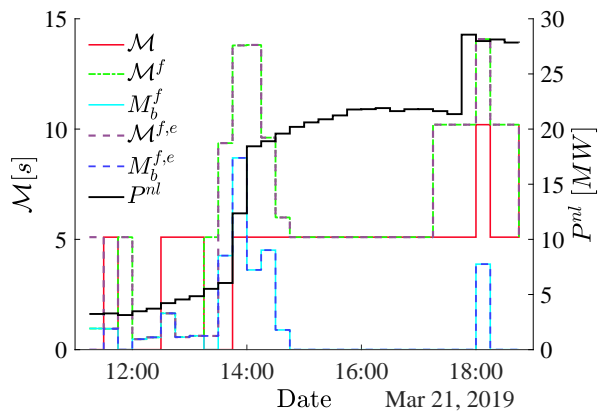


Fig. 4. Effect of the optimally calculated participation of the ESS in providing frequency support for a step load change when only 1 GT is on. In contrast with the case of non participation of the ESS to frequency regulation (solid and dashed grey lines), the optimally designed virtual inertia and damping results in a frequency response (solid black) and RoCoF (dashed black) that are bounded by their defined limit values.

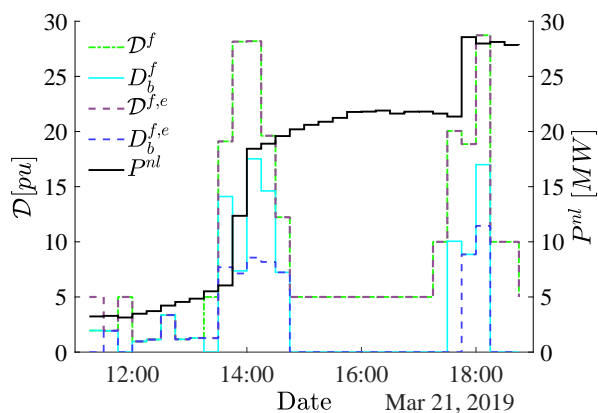
online GT is the only source of primary frequency control, while, in the second case (black lines), the ESS supports in this task the GT, which has the same droop setting as in the previous case. Observe that the system's response in the first case violates not only the steady-state frequency bound r_{ss} but also the maximum allowable RoCoF (\bar{r}), whereas in the second case both limits are respected. To respect the defined bound in the first case, the GT droop setting must be increased, leading to a larger deviation from the optimal GT operating point, decreased efficiency, increased fuel consumption and emissions. The same droop setting for the GT, on the other hand, can be maintained and the r_{ss} threshold observed where an optimal participation of the ESS in the primary frequency control (PFC) has been decided beforehand by the algorithm using an adaptive droop setting. Note also the compliance with the RoCoF limit where the ESS provides virtual inertia. To respect this limit without the ESS support would require an additional GT on, affecting significantly the overall efficiency of the system. The proposed algorithm, in other words, employs an adaptive droop and virtual inertia scheme, enabling not only the optimal scheduling of the power system by avoiding an additional GT on, but also guaranteeing that the services provided by the ESS to the grid will not cause it to deviate significantly from its optimal schedule, as the use of stored energy is bounded by Eq. (24). As a matter of fact, the calculated energy for frequency support provision by the ESS to the described disturbance for T (15 minutes) is 0.9179 MWh while the bound for $\lambda = 3\%$ is 0.9369 MWh.

C. Comparative analysis and effect of bounds

To further demonstrate the capabilities of the proposed EMS, a reference operation period is simulated considering: I) the default EMS that does not integrate any bounds; II) the version that includes frequency variation bounds but not the energy bounds on the ESS; and III) the proposed version which includes all of them.



(a) Total system inertia.



(b) Total system damping.

Fig. 5. Trajectories of the optimally designed system inertia (top) and damping (bottom) and optimal split between primary control provision by the GTs and the ESS for different bounds considerations. The simulated results are plotted against the net load signal (solid black) for a case where sudden step-like variations occur.

1) *System inertia and damping evolution:* The results for all EMS versions are aggregated in Fig. 5, being the system inertia and damping evolution depicted in Fig. 5a and Fig. 5b along with the net load signal $P_b^{nl}(t)$ (solid black line), during a reference period of 8 hours. No frequency and RoCoF containment reserves are considered in case I, the droop settings not being optimization variables and the ESS not contributing with virtual inertia. The system inertia $\mathcal{M}(t)$ (red line in Fig. 5a) is therefore just the result of the online GTs based on the optimal techno-economic scheduling, not having any virtual component $M_b(t)$. Following the same color notation in both Fig. 5a and Fig. 5b, the evolution of the system inertia and damping is observed, being the contribution of the ESS in case II denoted by the superscript f (frequency bound) and in case III by f, e (frequency and energy bound).

Two main patterns are evident when observing Fig. 5a and Fig. 5b. Firstly, more inertia and damping are assigned for both cases II and III close to the time instants of the sudden net load variations (around 14:00 and 18:00 correspondingly). Secondly, the same inertia and damping are noticed during the relatively constant net load conditions (between 14:00 and

TABLE I
PERFORMANCE COMPARISON FOR THE WHOLE SIMULATION PERIOD.

Performance indicator	Method		
	I	II	III
fuel consumption (ON GTs) [kg]	29,695	29,929	30,131
fuel costs (ON GTs) [€]	8,846	8,916	8,976
GTs ON time [$N_g \times T$]	27	31	31
GTs startup times [-]	5	4	5
ESS degradation [%]	0.164	0.148	0.165

18:00). This effect demonstrates the adaptive capabilities of the proposed EMS algorithm to assign more or less inertia and damping in correspondence with the anticipated net load variations. The larger the variations expected, the more secure the system will be by properly deciding its power and energy reserves. Whether the ESS is not assigned to frequency control, securing the system for possible net load variations would require additional GTs to be on. This is confirmed in Fig. 5a during both sudden net load variations, where $\mathcal{M}(t) \leq \mathcal{M}^f(t)$ (green line) and $\mathcal{M}(t) \leq \mathcal{M}^{f,e}(t)$ (magenta line). Note also that around those instants, $M_b^f(t) \geq 0$ (cyan line) and $M_b^{f,e}(t) \geq 0$ (blue line), meaning that the additional GT can be avoided by properly assigning virtual inertia to the ESS. Similar observations are drawn from Fig. 5b where $D_b^f(t) \geq 0$ (cyan line) and $D_b^{f,e}(t) \geq 0$ (blue line) around the sudden variation instants and $D_b^f(t) = 0$ and $D_b^{f,e}(t) = 0$ for the rest period.

Remark that the effect of the energy bounds on the ESS are stronger in the damping terms than in the inertia. Figure 5a shows that the signals $M_b^f(t)$ and $M_b^{f,e}(t)$ are almost identical for the whole time period, whereas Fig. 5b depicts that $\sup D_b^{f,e}(t) \leq \sup D_b^f(t)$. This means that the peak contribution of the ESS for case III is smaller than the one for case II. It is indeed possible to observe that $D_b^{f,e}(t)$ is almost always less than $D_b^f(t)$, further demonstrating that version III is more cautious not to overuse the PFC of the ESS.

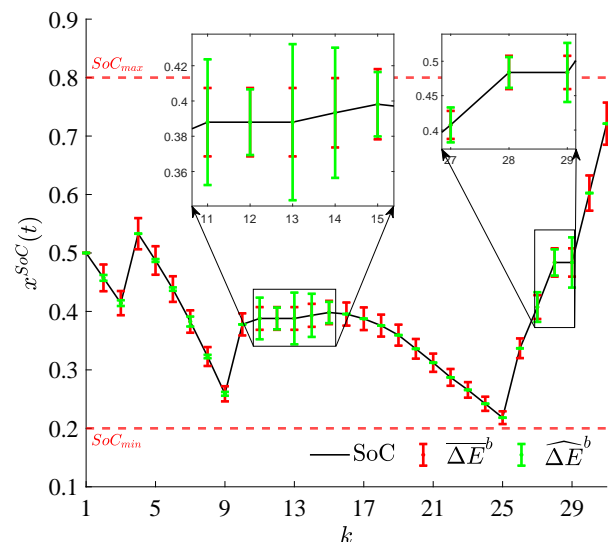
The comparison of the different methods (I, II, III) is also quantified through the cumulative results of specified key performance indicators in Table I. Including bounds on the EMS results in slightly higher fuel consumption and operating costs, which is primarily attributed to higher cumulative operational hours of the GTs. This agrees with the results presented in Fig. 5, as securing the system against possible disturbances may be associated with increased inertia requirements. The marginally increased fuel consumption of method III relatively to II (+0.7%) is justified by the bounded energy contribution of the ESS, which slightly moves the GTs away from their optimal reference setpoint. It is also noteworthy in Table I that the incremental cost for including bounds on the use of ESS stored energy (III) compared to case II is negligible, meaning that the optimal GT scheduling is almost not affected by the inclusion of energy bounds in the ESS. The main difference is that the resulting optimal GT trajectory for II is associated with one less GT start up compared to III and slightly lower ESS cycling, reflected on the lower degradation, which is however almost equal in cases I and III.

2) *State of charge evolution and energy bounds effect*: An additional comparison demonstrating the additional benefits coming from method III over method II is illustrated in Fig. 6. The resulting $x^{SoC}(t)$ signals from the application of II and III are depicted in Fig. 6a and Fig. 6b correspondingly. Notice that both methods respect the upper and lower state of charge limits, as originally designed in the default method I. Both trajectories seem to follow similar patterns, i.e. initial discharge until $k = 9$, smooth re-bouncing and discharge until $k = 25$, and charging until the end. There are however small but important differences, those being clearly depicted in the two zoomed areas ($k = 11 - 15$ and $k = 27 - 29$), where the maximum allowed energy deviation $\Delta E^b(t)$ from the frequency support offered by the ESS is illustrated with red error bars and the calculated upper bound $\widehat{\Delta E}^b$ is illustrated with green error bars. It is evident that, for case II, there would be requirements for the ESS that could cause it to violate the upper bound $\widehat{\Delta E}^b > \Delta E^b(t)$ at $k = 11, 14, 27, 29$, while the method in III controlled the ESS in a way that $\Delta E^b \leq \widehat{\Delta E}^b(t)$ is guaranteed for the whole period.

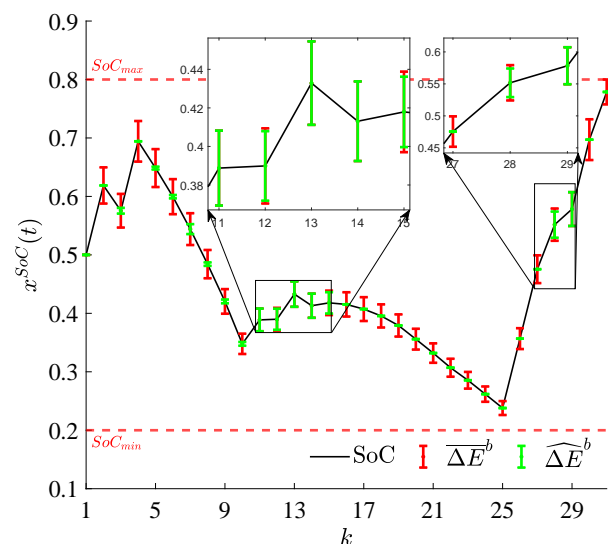
IV. CONCLUSIONS

Achieving optimal energy management in isolated power systems with energy storage and sudden load variations cannot be decoupled from ensuring their secure and robust operation, especially under the presence of intermittent renewable power sources. Even though decisions related to techno-economical operation are conventionally taken in the discrete time, those will inevitably affect the system's stability in its continuous operation and vice versa. To address this problem, this article proposed an energy management algorithm capable of integrating both higher time scale economic objectives and lower time scale stability constraints under adaptive uncertainty considerations. Additional constraints regarding the optimal use of the energy storage for providing flexibility and frequency support with bounded interaction between both services were proposed. A MILP formulation was derived and validated through time-domain simulations for an isolated offshore O&G platform integrating wind power. The results indicated that, under the proposed adaptive uncertainty framework, optimal decisions with dynamic frequency stability guarantees could be achieved and secured the system under an adaptive assessment of possible active power perturbations. This also reduced the conservatism from setting fixed damping and inertia requirements based on the expected worst-case and allowed better scheduling and operation of the GTs for longer periods. At the same time, the optimal sharing of primary frequency control contribution from conventional generators and the energy storage was found, while ensuring a tolerable impact on the storage optimal state of charge schedule and a negligible impact on the rest energy management objectives.

The presented method targeted a small scale APSs (an isolated offshore O&G platform), but the formulation is based on general principles and can potentially be applied to BPSs, where enough computational resources and proper assumptions (e.g., aggregation of regions/generator groups) are applied to solve the optimization problem within the scheduling



(a) Without bounds on the energy deviation.



(b) With bounds on the energy deviation.

Fig. 6. State of charge trajectories from the optimal scheduling and primary control design of the ESS, during the simulation period, for the cases of not including bounds on the resulting energy deviation from the participation in PFC (top) and the one when including the bounds (bottom).

period (i.e., 15 min.). Remark that, while possible configurations grow exponentially with the number of generators, a strong MILP structure is preserved in the proposed method, allowing an efficient solution of the resulting optimization problem. A topic for future research therefore may be verifying the applicability of the suggested algorithm to regional dispatch centers that can operate autonomously. From this perspective, a practical implementation in BPS also demands a standard framework for real-time command and telemetry of frequency reserves from the dispatch center to local primary controllers, which not only is a topic for future research but also should be addressed by regulatory and standardization bodies.

REFERENCES

[1] Y.-Y. Hong and G. F. D. Apolinario, "Uncertainty in Unit Commitment in Power Systems: A Review of Models, Methods, and Applications," *Energies*, vol. 14, no. 20, p. 6658, Jan. 2021.

[2] X. Xia and A. M. Elaiw, "Optimal dynamic economic dispatch of generation: A review," *Electr. Power Syst. Res.*, vol. 80, no. 8, pp. 975–986, Aug. 2010.

[3] B. Mohandes, M. S. E. Moursi, N. Hatzigiorgiou, and S. E. Khatib, "A Review of Power System Flexibility With High Penetration of Renewables," *IEEE Trans. Power Syst.*, vol. 34, no. 4, pp. 3140–3155, Jul. 2019.

[4] F. Dorfler, S. Bolognani, J. W. Simpson-Porco, and S. Grammatico, "Distributed Control and Optimization for Autonomous Power Grids," in *2019 18th European Control Conference (ECC)*. Naples, Italy: IEEE, Jun. 2019, pp. 2436–2453.

[5] Commission Regulation (EU) 2017/1485, "Guideline on electricity transmission system operation," Aug. 2017. [Online]. Available: <http://data.europa.eu/eli/reg/2017/1485/oj>

[6] E. F. Alves, L. Polleux, G. Guerassimoff, M. Korp as, and E. Tedeschi, "Allocation of spinning reserves for autonomous grids subject to frequency stability constraints and short-term solar power variations," *arXiv:2203.07233 [cs, eess]*, Sep. 2022.

[7] L. Sigrist, L. Rouco, and F. M. Echavarren, "A review of the state of the art of UFLS schemes for isolated power systems," *Intl. J. Electr. Power Energy Syst.*, vol. 99, pp. 525–539, Jul. 2018.

[8] J. Luo, F. Teng, and S. Bu, "Stability-Constrained Power System Scheduling: A Review," *IEEE Access*, vol. 8, pp. 219 331–219 343, 2020.

[9] V. Prakash, K. C. Sharma, R. Bhakar, H. P. Tiwari, and F. Li, "Frequency Response Constrained Modified Interval Scheduling Under Wind Uncertainty," *IEEE Trans. Sust. Energy*, vol. 9, no. 1, pp. 302–310, Jan. 2018.

[10] Q. Shi, F. Li, and H. Cui, "Analytical Method to Aggregate Multi-Machine SFR Model With Applications in Power System Dynamic Studies," *IEEE Trans. Power Syst.*, vol. 33, no. 6, pp. 6355–6367, Aug. 2018.

[11] L. Badesa, F. Teng, and G. Strbac, "Simultaneous Scheduling of Multiple Frequency Services in Stochastic Unit Commitment," *IEEE Trans. Power Syst.*, vol. 34, no. 5, pp. 3858–3868, Sep. 2019.

[12] V. Trovato, A. Bialecki, and A. Dallagi, "Unit Commitment With Inertia-Dependent and Multispeed Allocation of Frequency Response Services," *IEEE Trans. Power Syst.*, vol. 34, no. 2, p. 12, 2019.

[13] Z. Zhang, E. Du, F. Teng, N. Zhang, and C. Kang, "Modeling Frequency Dynamics in Unit Commitment With a High Share of Renewable Energy," *IEEE Trans. Power Syst.*, vol. 35, no. 6, pp. 4383–4395, Aug. 2020.

[14] S. S. Oskouee, S. Kamali, and T. Amraee, "Primary Frequency Support in Unit Commitment Using a Multi-Area Frequency Model With Flywheel Energy Storage," *IEEE Trans. Power Syst.*, vol. 36, no. 6, pp. 5105–5119, Aug. 2021.

[15] T. Ding, Z. Zeng, M. Qu, J. P. S. Catal ao, and M. Shahidehpour, "Two-Stage Chance-Constrained Stochastic Thermal Unit Commitment for Optimal Provision of Virtual Inertia in Wind-Storage Systems," *IEEE Trans. Power Syst.*, vol. 36, no. 4, pp. 3520–3530, Jul. 2021.

[16] V. Trovato, "System Scheduling with Optimal Time-varying Delivery Intervals for Frequency Response," *IEEE Trans. Power Syst. (Early Access)*, Feb. 2022.

[17] E. Alves, G. Bergna-Diaz, D. Brandao, and E. Tedeschi, "Sufficient Conditions for Robust Frequency Stability of AC Power Systems," *IEEE Trans. Power Syst.*, vol. 36, no. 3, pp. 2684–2692, May 2021.

[18] H. Ahmadi and H. Ghasemi, "Security-Constrained Unit Commitment With Linearized System Frequency Limit Constraints," *IEEE Trans. Power Syst.*, vol. 29, no. 4, pp. 1536–1545, Jul. 2014.

[19] Y. Wen, W. Li, G. Huang, and X. Liu, "Frequency Dynamics Constrained Unit Commitment With Battery Energy Storage," *IEEE Trans. Power Syst.*, vol. 31, no. 6, pp. 5115–5125, Aug. 2016.

[20] C. Zhang, L. Liu, H. Cheng, D. Liu, J. Zhang, and G. Li, "Frequency-constrained Co-planning of Generation and Energy Storage with High-penetration Renewable Energy," *J. Mod. Power Syst. Clean*, vol. 9, no. 4, pp. 760–775, Jul. 2021.

[21] C. Cardozo, L. Capely, and P. Dessante, "Frequency constrained unit commitment," *Energy Syst*, vol. 8, no. 1, pp. 31–56, Feb. 2017.

[22] M. Javadi, T. Amraee, and F. Capitanescu, "Look ahead dynamic security-constrained economic dispatch considering frequency stability and smart loads," *Intl. J. Electr. Power Energy Syst.*, vol. 108, pp. 240–251, Mar. 2019.

[23] Y. Yin, T. Liu, L. Wu, C. He, and Y. Liu, "Frequency-constrained multi-source power system scheduling against N-1 contingency and renewable uncertainty," *Energy*, vol. 216, p. 119296, Oct. 2021.

[24] A. Safari, M. Farrokhifar, H. Shahsavari, and V. Hosseinnezhad, "Stochastic planning of integrated power and natural gas networks with simplified system frequency constraints," *Intl. J. Electr. Power Energy Syst.*, vol. 132, p. 107144, Aug. 2021.

[25] M. Carri on, R. Z arate-Mi ano, and F. Milano, "Impact of off-nominal frequency values on the generation scheduling of small-size power systems," *Intl. J. Electr. Power Energy Syst.*, vol. 122, p. 106174, Aug. 2020.

[26] IEEE Task Force on Turbine-Governor Modeling, "Dynamic Models for Turbine-Governors in Power System Studies," IEEE, New York, NY, Technical Report PES-TR1, Aug. 2013.

[27] S. Chapaloglou, D. Varagnolo, F. Marra, and E. Tedeschi, "Data-driven energy management of isolated power systems under rapidly varying operating conditions," *Appl. Energy*, vol. 314, p. 118906, May 2022.

[28] L. Breiman, "Random Forests," *Machine Learning*, vol. 45, pp. 5–32, Oct. 2001.

[29] N. Meinshausen, "Quantile Regression Forests," *The Journal of Machine Learning Research*, vol. 7, pp. 983–999, Dec. 2006.

[30] E. F. Camacho and C. Bordons, *Model Predictive control*, ser. Advanced Textbooks in Control and Signal Processing, M. J. Grimble and M. A. Johnson, Eds. London: Springer London, 2007.

[31] M. Vrakopoulou, K. Margellos, J. Lygeros, and G. Andersson, "A Probabilistic Framework for Reserve Scheduling and $\{N\}$ -1\$ Security Assessment of Systems With High Wind Power Penetration," *IEEE Trans. Power Syst.*, vol. 28, no. 4, pp. 3885–3896, Nov. 2013.

[32] K. Hreinsson, M. Vrakopoulou, and G. Andersson, "Stochastic security constrained unit commitment and non-spinning reserve allocation with performance guarantees," *Intl. J. Electr. Power Energy Syst.*, vol. 72, pp. 109–115, Aug. 2015.

[33] K. Margellos, P. Goulart, and J. Lygeros, "On the Road Between Robust Optimization and the Scenario Approach for Chance Constrained Optimization Problems," *IEEE Trans. Automat. Contr.*, vol. 59, no. 8, pp. 2258–2263, Aug. 2014.



Spyridon Chapaloglou received the Diploma in Mechanical Engineering, and the M.Sc. degree in Automation Systems from the National Technical University of Athens (NTUA), Greece, in 2016 and 2018, respectively. He is currently working towards the Ph.D. degree with the Department of Electric Power Engineering at the Norwegian University of Science and Technology, Trondheim, Norway. His research interests include stochastic optimization and predictive control for isolated power systems, energy management under uncertainty, energy storage sizing, and data-driven/statistical methods applied to power systems. Since 2022 he has also joined Sintef Energy, Trondheim, Norway, working as a research scientist on offshore energy systems.



Erick F. Alves (S'06–M'08–SM'19) received the B.E. in energy and automation from the University of S ao Paulo, SP, Brazil, in 2007, and the M.S. degree in electrical engineering from the Arctic University of Norway, Narvik, Norway in 2018. Since 2018, he has been pursuing the Ph.D. degree with the Department of Electric Power Engineering at the Norwegian University of Science and Technology, Trondheim, Norway. His research interests includes optimal and model predictive control, energy storage systems, ac micro-grids, power electronics for renewable and distributed power systems, electrical machines, excitation systems, and condition monitoring. Mr. Alves is a member of the IEEE Standards Association, CIGR E, and held several positions (Chair, Vice-chair, Treasurer) with the IEEE Power and Energy Chapter in Norway.



Vincenzo Trovato (M'15) is an Assistant Professor at the University of Trento, Italy and an Honorary Research Fellow at the Imperial College London, UK. Previously, he was Policy Officer at EU ACER, Research Engineer at EDF R&D and Research Associate at Imperial College London where he obtained the Ph.D. degree in Electrical Engineering. He also owns a M.Sc. Degree in Electrical Engineering from Politecnico di Torino, Italy and a B.Sc. Degree in Electrical Engineering from Politecnico di Bari, Italy. His current research is focused on modeling

and optimization of economic and security performance of energy system operation and investment, including analysis of future energy markets to support cost-effective transition to smart low carbon energy future.



Elisabetta Tedeschi (Senior Member, IEEE) received the M.Sc. degree (Hons.) in electrical engineering and the Ph.D. degree in industrial engineering from the University of Padua, Italy, in 2005 and 2009, respectively. From 2009 to 2011, she was a Postdoctoral Researcher with the Norwegian University of Science and Technology (NTNU), working on the grid integration of offshore renewable energies. She was a Researcher/Marie Curie Fellow at Tecnalia, Spain, from 2011 to 2013, where she worked as the Principal Investigator in the FP7-Sea2grid

Project, related to the storage needs for the grid integration of wave energy converters. From 2013 to 2014, she was a Research Scientist at SINTEF Energy, and an Adjunct Associate Professor at NTNU. In 2014, she became a Full Professor within the offshore grid at NTNU. Since 2020, she has also been a Full Professor at the Department of Industrial Engineering of the University of Trento, Italy. She has a core competence in the design and control of energy conversion and transmission and distribution systems, with a focus on offshore energy and power-quality issues. She has led and/or contributed to more than 15 national and international scientific projects and she has authored or coauthored two book chapters and more than 150 journals and conference papers in the field of marine energy and energy conversion systems.